On predicting offshore hub-height wind speed and wind power density in the Northeast US coast using high-resolution WRF model configurations during anticyclones coinciding with wind drought

5 Tasnim Zaman[1], Timothy W. Juliano[2] and Patrick Hawbecker[3], Marina Astitha[1,2]

[1]Department of Civil and Environmental Engineering, University of Connecticut, Storrs, CT, United States
[2]National Center for Atmospheric Research (NCAR), Research Applications Laboratory, Boulder, CO
[3]ArcVera Renewables, Golden, CO

10 *Correspondence to*: Marina Astitha (marina.astitha@uconn.edu)

Abstract. We investigated the predictive capability of various configurations of the Weather Research and Forecasting (WRF) model version 4.4, to predict hub-height offshore wind speed and wind power density in the Northeast US wind farm lease areas. The selected atmospheric conditions were high-pressure systems (anticyclones) coinciding with wind speed below the

15 cut-in wind turbine threshold. There are many factors affecting the potential of offshore wind power generation, one of them being low winds, namely wind droughts, that have been present in future climate change scenarios. The efficiency of high-resolution hub-height wind prediction for such events has not been extensively investigated, even though the anticipation of such events will be important in our increased reliance on wind and solar power resources in the near future. We used offshore wind observations from the Woods Hole Oceanographic Institution's (WHOI) Air-Sea Interaction Tower (ASIT) tower located

20 south of Martha's Vineyard to assess the impact of initial and boundary conditions, number of model vertical levels, and inclusion of high-resolution sea surface temperature (SST) fields. Our findings showed that the initial and boundary conditions exhibited the strongest influence on hub height wind predictions above all other factors, such as SST and model vertical layers. NAM/WRF and HRRR/WRF were able to capture the decreased wind speed, and there was no single configuration that systematically produced better results. However, when using the predicted wind speed to estimate wind power density,

25 HRRR/WRF had statistically improved results, with lower errors than NAM/WRF. Our work underscored that for predicting offshore wind resources, it is important to evaluate not only the WRF predictive wind speed, but also the connection of wind speed to wind power.

1 Introduction

Offshore wind is an abundant energy resource with significant environmental and economic benefits. When it comes to

30 assessing the magnitude of wind produced over the sea compared to land surface, offshore wind outperforms due to it being less impacted by topographical influences like surface roughness and low turbulence (Pryor and Barthelmie 2002; Aird et al. 2022). Quantifying wind in the lowest part of the atmospheric boundary layer is a challenge due to the combination of forcing produced from friction and vertical motion due to heat over the surface that affect wind formation (Yoo et al. 2012; Ryu et al.

2016). Compared to land, the ocean produces a larger amount of water vapor that is transferred into the atmosphere, and the
35 heat budget also differs which affects the atmospheric stability conditions (Archer et al. 2016). As a result of being strongly impacted by the atmospheric stability associated with turbulence exchange and interaction with the ocean waves, the offshore wind shear profile is often complicated (Aird et al. 2022; Vickers and Mahrt 1999).

The operational efficiency of offshore wind farms relies on highly accurate information, and thus high-quality measurements, of wind and waves, which is a challenge due to the lack of routine atmospheric measurements (Colle et al. 2016; Optis et al.
40 2021). To fill the gap of inadequate measurements, numerical weather prediction (NWP) models are used to predict atmospheric conditions at fine spatial and temporal scales. While many current studies apply NWP models to predict wind for wind energy farms located both offshore and onshore, there are some challenges that have been identified particularly for the offshore region (Banta et al. 2017; James et al. 2017). Complexities arise due to land-ocean interactions, the formation of low-level jets, the dynamic nature of ocean-atmosphere waves and high wind shear due to stable boundary layer over the ocean as
45 warm air from the land rapidly moves toward the relatively cold ocean water (Li et al. 2021, Floors et al., 2013, Nunalee and Basu, 2014, Svensson et al., 2019a, Svensson et al., 2019b, Hallgren et al., 2020).

According to the Offshore Wind Market report 2023 edition, the United States (U.S.) offshore wind energy project development and operational pipeline grew to a potential generating capacity of 52,687 megawatts (U.S. DOE, 2023) in 2022. Further, a national goal set in March 2023 of 112,286 MW of offshore wind energy is expected to be in line with global growth
50 patterns by 2050. The Mid-Atlantic Bight has recently seen heavy investment in offshore wind power farms, with most installations still ongoing or planned in the next few years, as of this writing (Musial et al., 2021). Offshore wind farms must be designed to withstand extreme weather including tropical storms, extreme wind/wave events, icy conditions, extreme heat or cold. In addition, wind drought (very low wind occurrences) is an extreme condition that hinders the energy production capacity of wind farms (Novacheck et al. 2021). Given the plan by most NE U.S. States to move to 100% clean energy by
55 2040 to 2050 (Clean Energy States Alliance website, accessed Sep 2023), we expect increasing reliance on renewable resources in the near future. Climate assessment studies point to a potential future decrease of wind speed and wind power density for the offshore region of the NE U.S. (Pryor et al. 2012; Liu et al. 2014; Johnson and Erhardt, 2016; Costoya et al. 2020; EPRI 2021; Martinez and Iglesias, 2022), which could affect wind power generation reliability. Anticipating, and, thus, reliably predicting such wind drought offshore conditions, would be beneficial for the wind power industry and utility operators.
60 The efficiency of high-resolution hub-height wind prediction for such events has not been extensively investigated. Moreover, due to the relationship between wind power density and cubed wind speed, small changes in wind speed prediction will lead to important changes in wind power density prediction. We investigated the performance of a high-resolution NWP model that can address the mentioned challenges, focusing on the U.S. Northeast Atlantic region. To apply a high-resolution mesoscale (horizontal grid cell spacing, dx = 600m) model suitable for predicting offshore wind at vertical height
65 corresponding to the wind turbine hub level, we performed multiple sensitivity simulations using the Weather Research and Forecasting (WRF; Skamarock et al. 2019) model version 4.4. Domain configurations with multiple nested domains, variations in initial and boundary conditions, number of model vertical layers, and sea surface temperature fields have been explored.

While designing and analyzing the modeling experiments, the following questions were considered: What is the impact of initial and boundary conditions, and number of vertical layers for the prediction of offshore hub height wind during anticyclonic conditions? How important is an accurate representation of the sea surface temperature (SST) field in WRF to accurately depict hub height wind? How is wind power density affected by changes in predicted hub height wind? These questions guide our assessment of the WRF model's efficiency to accurately predict offshore wind speed over the Northeast US cluster of wind farm lease areas. The long-term goal is to be able to accurately forecast conditions of wind extremes, in both sides of the spectrum, low and high winds that affect offshore wind turbine operations.

2 Materials and Methods

2.1 WRF Model Configuration

The WRF v4.4 model, which for many years has been a useful tool for operations and research (Skamarock et al. 2005, 2008, 2019), is applied here with two different initial and boundary conditions and two-way nested domains with the finest domain having dx = dy = 600m (Fig. 1). We chose the dynamic solver Advanced Research WRF (ARW), which uses a fully compressible, non-hydrostatic Euler equation and consists of a vertical coordinate system with terrain-following hydrostatic-pressure (Skamarock et al. 2019). Our project is a partnership with Eversource-Orsted focusing on the South Fork Wind Farm (SFWF) in the Northeast US coast. The relatively high model resolution is chosen due to our collaboration with the research group that has developed the University of Connecticut's large-eddy simulation model to depict wind turbines at a very fine scale (Matheou et al. 2022), using the WRF output as initial and boundary conditions to the LES model.

For the domain selection, we considered available offshore observations covering the north-east U.S. coastline, especially near the South Fork Wind Farm (Fig. 1). The parent domain had an equal ratio of covering both land and ocean to observe the interaction of land and ocean with the atmosphere. The initial sensitivity tests revealed two datasets as the preferred ones for the initial and boundary conditions: the North American Mesoscale Forecast System (NAM) (Environmental Modeling Center, National Centers for Environmental Prediction, National Weather Service, NOAA, U.S. Department of Commerce) and the High-Resolution Rapid Refresh (HRRRv3) (Benjamin et al., 2016) (Fig. 1 and Table 1). The choice of these two modeling systems is based on the intention to deploy the WRF model operationally in the near future, and we needed to test modeling systems that can be used in forecast mode while offering sufficient high-resolution outputs. Both WRF configurations use the same physics parameterizations. The NAM/WRF configuration has three domains as the model had to dynamically downscale data from a coarse resolution of 12 km to 5.4km, 1.8km, and further 600m. The HRRR/WRF configuration has two domains since downscaling needed to be performed from 3 km to 1.8km and 600m. We tested two sets of vertical levels for both initializations: (a) 56 vertical levels with 10 levels within 200m and stretched above, and (b) 131 vertical levels with 21 levels (10m intervals) up to ~400m. For the rest of the article, we will refer to each configuration as NAM/WRF and HRRR/WRF for simplicity.

100

Table 1: WRF model configuration

|		
Numerical Weather Prediction Model	WRF v4.4	
Initial/boundary conditions	• The North American Mesoscale Forecast System (NAM) 12km (every 6h) • The High-Resolution Rapid Refresh (HRRRv3) 3km (every 6h)	
Grid Structure	**Test 1 (with NAM):** 5.4km (D01), 1.8km (D02) and 600m (D03)	**Test 2 (with HRRR):** 1.8km (D01) and 600m (D02)
Vertical levels	**Test 1:** 56 vertical levels (Ptop = 50 hPa, 10 levels up to ~200m)	**Test 2:** 131 vertical levels (Ptop = 50 hPa, 21 levels up to ~400m)
Cloud Microphysics scheme	Thompson et al. (2008)	
Planetary Boundary Layer	Yonsei University scheme (Hong et al. 2006)	
Radiation scheme	Goddard for shortwave radiation (Chou and Suarez 1994) RRTM for longwave radiation (Mlawer et al. 1997)	
Land surface scheme	Noah LSM (Niu et al. 2011)	

105
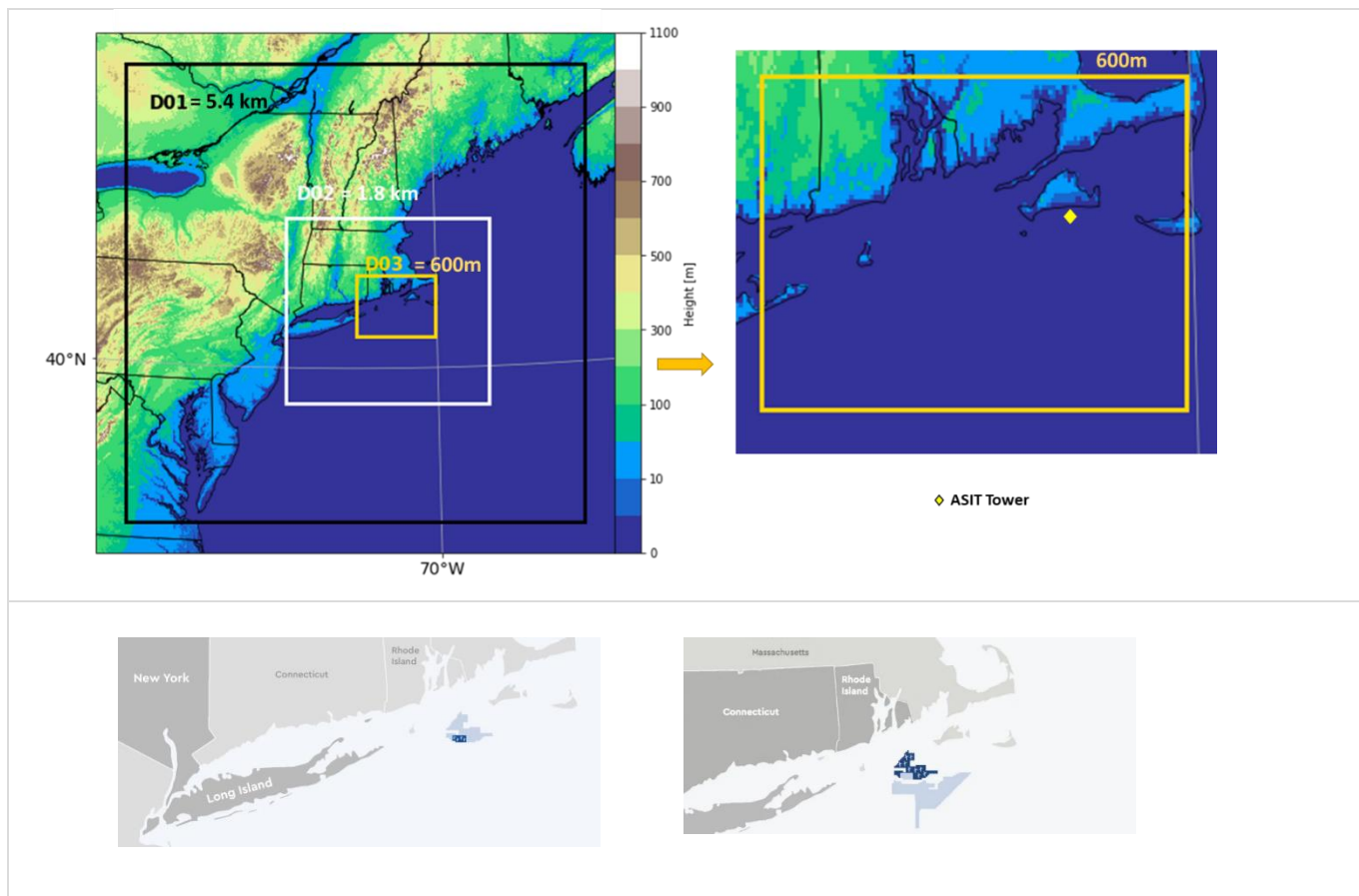
Figure 1: (Top row) WRFv4.4 model domains and location of the ASIT tower. (Bottom row) Location of South Fork Wind (left) and Revolution Wind (right) leased areas (taken from https://southforkwind.com/ and https://revolution-wind.com/).

2.2 Offshore Observations

110   Historically, there have been more wind observations available up to the turbine hub height inland than offshore. With the increase of offshore wind farm developments in the Mid-Atlantic Bight, lidar buoys have been deployed to ensure the timely characterization of atmospheric condition. Our study area covers the cluster of leased wind farm areas in the Northeast US (South Fork Wind and Revolution Wind; Fig. 1). There is no lidar buoy deployed in that area that provides free accessible data. To alleviate this observational gap, we used the Woods Hole Oceanographic Institution's (WHOI) Air-Sea Interaction

115   Tower (ASIT) (Filippelli et al., 2015; Bodini et al. 2019). Wind observations are available from anemometers located at 26m AMSL (above mean sea level) and a single wind direction vane located at 23m AMSL, as well as additional sensor data of air temperature, pressure, and relative humidity at 18m AMSL and ocean temperature and salinity at 4m BMSL (below mean sea level). More importantly, a lidar (WLS7-436) placed at the tower's platform level, provided wind observations up to 187m AMSL (Kirincich et al. 2020).

120 In terms of evaluating the model's accuracy in forecasting offshore wind, one of the key factors is SST, as it has a direct impact on atmospheric stability conditions. Though WRF can use the SST input from the relatively coarse initialization data, previous studies like Redfern et al. (2023) and Hawbecker et al. (2022), have performed simulations with external SST inputs which have higher resolution compared to the initial and boundary conditions (ICs and BCs). They have observed that the differences in both temporal and spatial resolution between SST products have an impact on wind speed characterization, with higher

125 resolutions tending to enhance model performance. We have compared the following SST datasets: the 0.01° Multiscale Ultrahigh Resolution (MUR), the 0.054° Office of Satellite and Product Operations (OSPO) analysis, the 0.054° Operational Sea Surface Temperature and Sea Ice Analysis (OSTIA), the 1° Naval Oceanographic Office (NAVO) and the 0.02° Geostationary Operational Environmental Satellites (GOES-16) dataset, to find the SST that is closer to the observations. As the externally available SST products have resolutions ranging from 0.1 degree to 1 degree, our tests showed that OSPO was

130 closest to the observed SST, and we chose to use this product and compare with the SST values from NAM and HRRR. Details will be discussed in section 3.3.

2.3 Statistical evaluation metrics

The statistical metrics of interest are systematic and random components of the model error (bias, Root-mean-squared-error (RMSE), Centered-root-mean squared-error (CRMSE)). Table 2 lists the formulas for each error metric. We also calculated

135 95th percentile confidence intervals for each error metric through bootstrapping (10,000 bootstrap samples with random replacement).

140

145

150

Table 2: Statistical Error Metrics

Error Metrics	Equation
mean BIAS	$$mean\ BIAS = \sqrt{\frac{1}{N}\sum_{n=0}^{N} P_n - O_n}$$ P_n and O_n represent the model prediction and observation, where N is the number of available data.
Root-mean-squared-error (RMSE)	$$RMSE = \sqrt{\frac{1}{N}\sum_{n=0}^{N} (P_n - O_n)^2}$$ The RMSE consists of both systematic and random error components (bias and CRMSE) (Taylor 2012). $$RMSE = \sqrt{BIAS^2 + CRMSE^2}$$
Centered-root-mean squared-error (CRMSE)	$$CRMSE = \sqrt{\frac{1}{N}\sum_{n=0}^{N}\left[(P_n - P_{avg}) - (O_n - O_{avg})\right]^2}$$ CRMSE describes the centered pattern of the error, the differences in wind speed variations around the mean. P_{avg} and O_{avg} represent the model prediction and observation averages over the number of available data, N values.

2.4 Selection of Events

155

Previous studies performed over offshore region like Kempton et al. (2010) presented multiple scenarios explaining the impact of synoptic-scale circulation on wind power production. They showed that high winds are found mostly at locations with the highest surface pressure gradients, with weaker winds observed at the core of the high-pressure system. According to the DOE Office of Energy Efficiency & Renewable Energy, a wind velocity at the turbine height between 6 and 9 mph (2.7-4 m/s) is a

160 typical range needed to drive wind turbines (or 3 m/s according to Zeng et al. 2019), but the duration of wind at that cut-in rate is equally important.

Self-Organizing Maps (SOMs) are used to objectively select cases that would be simulated with WRF. The SOMs algorithm, developed by Kohonen at al. (1995), is a type of unsupervised artificial neural network, used for clustering data and performing pattern identification. SOMs create structured maps with contiguous nodes holding similar data based on the number of

165 nodes/matrixes the user selects. To begin a SOM, initialization weight vectors are assigned to the connections/nodes with input vectors. The initialization process employs principal component analysis, which evenly distributes weights depending on the

two greatest principal component eigenvectors of the input data (Ciampi & Lechevallier, 2000; Wang et al., 2022). Based on Euclidean distance, nodes compete to claim input vectors and winners are selected upon minimum distance. The weight vectors of the winning node and its neighbors keep updating to match the input patterns and final maps are generated through multiple iterations (Stauffer et al., 2016; Juliano et al., 2020; Wang et al., 2022).

We have used an open-source Python package, minisom (Vettigli, 2018), to create the maps. For input data, we used the normalized (spatial anomaly, data was normalized by subtracting the mean from each array) 00z geopotential height field at 850-hPa over the year 2020 from HRRR 3km data (Benjamin et al., 2016). The total number of input vectors was 366 and for the training we used 1000 iterations. We have selected geopotential height as our input vector as it can provide valuable information regarding atmospheric circulation. Sensitivity tests with different SOM node configurations (Fig. 2) helped define a suitable number of nodes. We have compared the topographic error (TE) and quantization error (QE) for each combination. QE is a measure of how well a map resembles the original data and is computed by averaging the distance between each input data point and its closest representative node on the map. As the number of nodes increases, QE decreases. On the other hand, the preservation of spatial links between data points on a map is evaluated by TE. The percentage of input data points for which the first and second best-matching nodes on the map are not neighbors is known as topographic error, and it can be used to determine how well the map preserves the topological structure of the data. A lower topographic error indicates greater data topological retention (Juliano et al., 2020; Wang et al., 2022). Apart from the error values, we also considered availability of sufficient sample size in each node and based on all these criteria, we have selected the 3x4 matrix with 12 nodes, where we have around 5% or more samples in each node (Fig. 3).

We selected two nodes (7 and 12) that are characterized by relatively weak forcing (Fig. 3). From each node we have selected two events: August 20-22 and November 8-10, 2020, from Node 7. May 20-22 and June 15-17, 2020, from Node 12. Each of the selected events had a high-pressure system present throughout the 48-hour evaluation period (which excluded a 12-hour model spin-up time) of the simulated event. Additionally, the persistence of the high-pressure system did not extend beyond the event period.
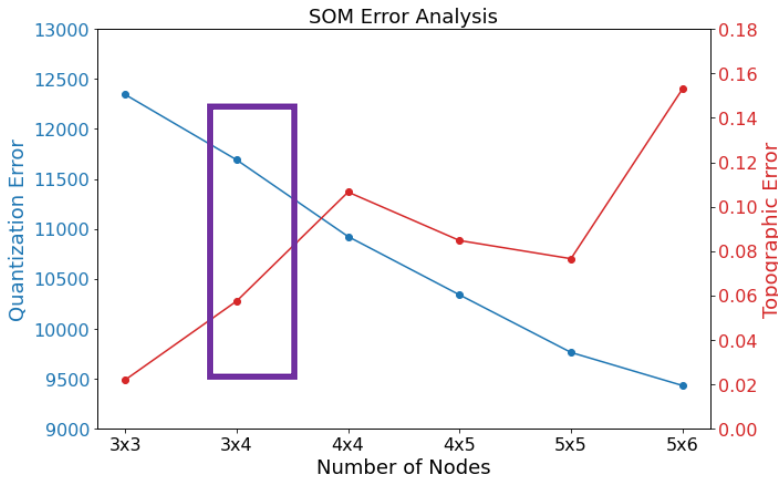
205

210

Figure 2: Comparing errors for different numbers of SOMs nodes. The purple rectangle indicates our selected matrix suitable for the study.
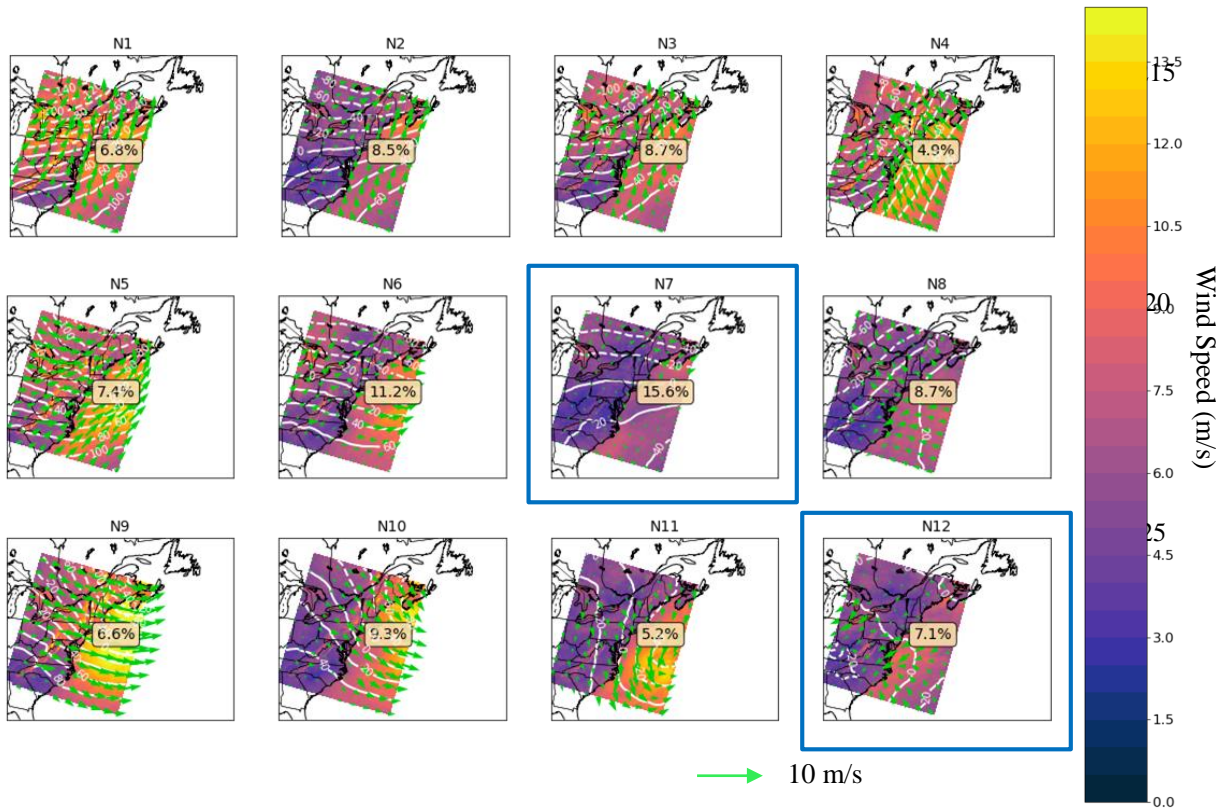

230

Figure 3: Self Organizing Maps (SOMs) created using spatial anomaly of the geopotential height field at 850hpa from HRRR analyses simulations for the year 2020. The plots are showing wind speed at 80m AMSL with wind direction. We also show the percentage of samples that falls within each node, and highlight the two nodes, N7 and N12, that we focus on in this study.

235   Regarding the high-pressure system location and occurrence time, we have consulted the surface analysis synoptic maps produced by NOAA's Weather Prediction Center (Fig. 4) to confirm our SOM results. According to the synoptic maps, a persistent high-pressure system with 1032 mb central pressure is observed near Martha's Vineyard throughout the event that took place on May 20. The core of the anticyclone is positioned over the New England coast, where the wind speed decreases below 5 m/s (Fig. 4, May 21, 2020, 12UTC). On June 15, a high-pressure system with the highest recorded pressure of 1029

240   mb, was positioned over the Great Lakes, with its extension influencing the location of the ASIT tower. Like the May event, a high-pressure system reaching 1017 mb was recorded on August 21 over the New England coast. The anticyclone is not as well organized as the May one, and the wind speed at the hub height did not exhibit the same decrease as shown in the wind speed time series that follow in Fig.5. The wind speed decrease for the May event was about 8 m/s within 18 hours, while for the August event the decrease is about 5 m/s within 9 hours (according to the time series presented in section 3.1). On

245   November 8, a well-organized high-pressure system with a peak pressure reading of 1024 mb, was located over Pennsylvania, influencing the New England coast. The anticyclone moved east and over the Atlantic. During all these high-pressure systems, the ASIT tower observed a decrease in wind speed and a shift in wind direction for three of the systems.
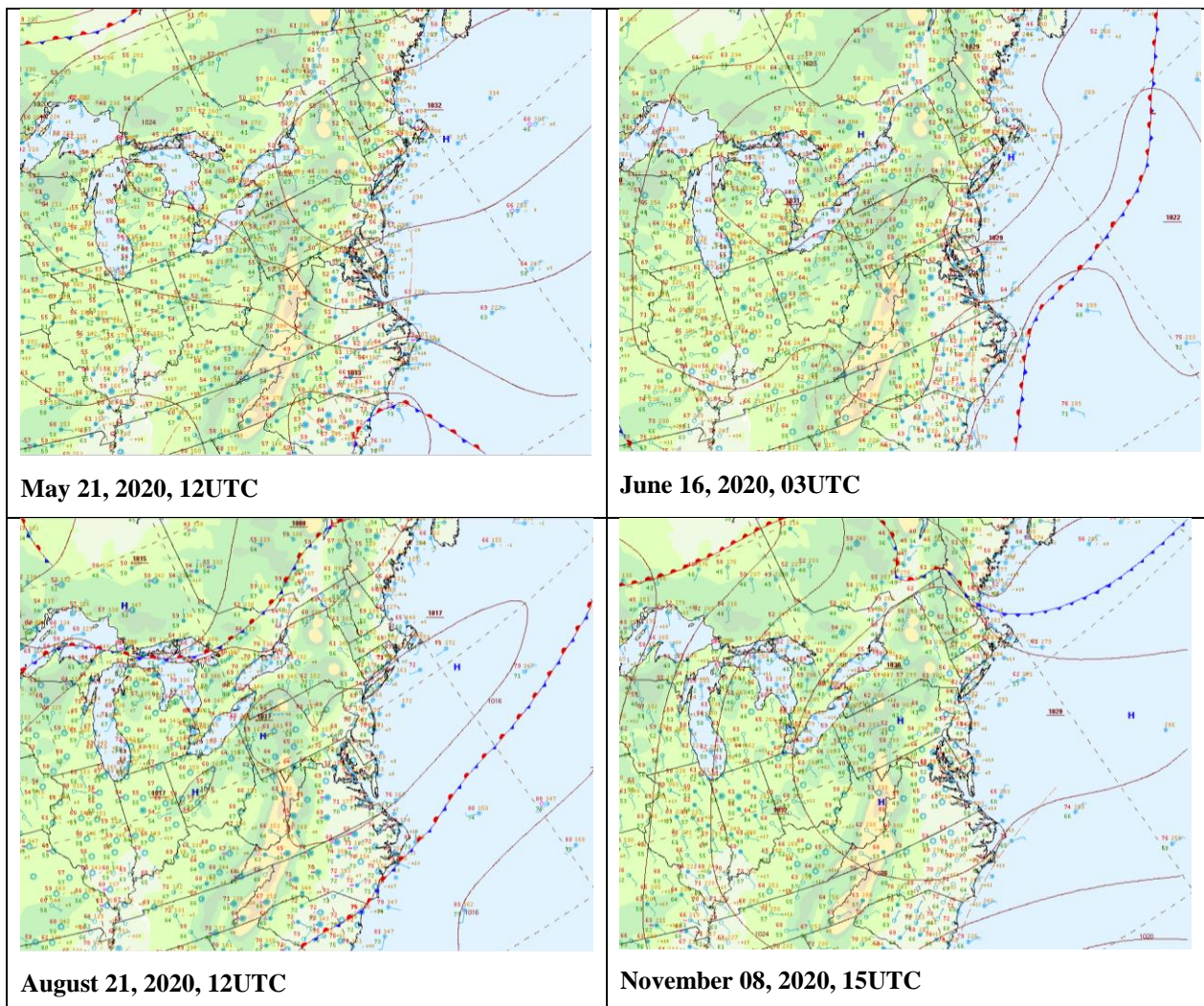

250

255

May 21, 2020, 12UTC

June 16, 2020, 03UTC

August 21, 2020, 12UTC

November 08, 2020, 15UTC

Figure 4: Surface Analysis maps from NOAA's Weather Prediction Center (https://www.wpc.ncep.noaa.gov/).

260 3 Results and Discussion

In the following sections, we examine the performance of the various WRF configurations for sensitivity to initial and boundary conditions, vertical levels, SST inputs, and influence on prediction of wind power density.

3.1 Influence of Initial and Boundary conditions

In this section we discuss the hub height wind prediction for the four anticyclones due to the influence of initial and boundary 265 conditions. We have created time series plots of wind speed and wind direction at the closest available observation height of the wind turbine hub height (Fig. 5). The wind turbine hub height is 140m AMSL (Dr. Astitha's personal communication with

Orsted, July 2023, site under construction), so we performed model evaluations at the lidar's height that is closest to the hub height by interpolating the model to 147m (ASIT tower lidar measurement height).

A major concern when conducting NWP simulations at grid spacing below ~1km is the impact of the turbulence gray-zone, or
270 Terra Incognita (Wyngaard 2004). According to Rai et al. (2019) and Haupt et al. (2022), the planetary boundary layer depth is the maximum limit of the terra incognita, meaning that horizontal spacing smaller than the boundary layer depth (but greater than around 100 m) is likely to produce fictitious secondary structures. For the events on August 20th, November 8[th,] and May 20th, the modeled PBL height at the location of the lidar buoy was nearly always lower than the horizontal grid spacing of 600m (Fig. 5). Such an outcome supported findings from previous studies that showed no impact of Terra-incognita when the
275 PBL height is less than the horizontal grid spacing (Δx) but greater than 100m (Rai et al. 2019; Haupt et al. 2022) and provided confidence in our use of the 600m gridded domain results.

The time series plots highlighted that both model configurations for the four different anticyclonic events captured the temporal evolution of wind speed at the hub height quite well (Fig. 6). Both model configurations struggled to capture the November event, which exhibited a steady upward trend of wind speed, though NAM/WRF reached the peak at the very end of the
280 simulation. Also, there was sudden and frequent shift in wind direction which prevailed from the northwest, but as wind speed dropped, the wind direction changed to become southward, ultimately settling into a southwesterly direction over time. Neither model could capture the clear westerly wind seen in the observations. In the May event, the wind was initially northeast and then shifted to a south-southeasterly direction due to the influence of the transition of high pressure. The models captured the transition very well. In June, a northeast wind was predominant, which the models represented accurately. Finally, during the
285 August event, winds were predominantly south-southwesterly, briefly shifting to northwesterly at the end of the event. Particularly, during the drop of wind speed, HRRR/WRF tended to portray the change in wind direction closer to the observations.

Hub height winds, for the four anticyclones, were, for the most part, below the rated power wind speed for the South Fork wind farm, which is ~ 12m/s (Dr. Astitha's personal communication with Orsted, September 2023). This is the wind speed
290 that the wind turbine will start producing its maximum constant power (or rated power), until, and if, the wind reaches a cut-out speed (varies by turbine). There are many consecutive hours in the individual four 48-hr events, where the wind power generation would be highly variable (from the cut-in speed until 12m/s) or zero (when the wind is less than the cut-in wind speed) (Fig. 6). According to the New York State Wind Energy Guidebook, typically, wind turbines start producing electricity at wind speeds of about 6.7 mph (3 m/s), which is the value we used in our study. The wind turbine's performance would be
295 hindered when faced with reduced wind speeds, such as during the high-pressure systems we have analyzed, and being able to forecast them well in advance would be essential for wind farm operators and power utilities.

The performance of HRRR/WRF was significantly better than NAM/WRF for the May and August anticyclones regarding RMSE and CRMSE (Fig. 7). Note that we used CRMSE to determine the discrepancies between modeled and observed values that are due to random processes, and hence difficult to reduce. The May and August cases were very similar in the geographic
300 positioning of the high-pressure system, which HRRR/WRF captured better than NAM/WRF. The systematic error (mean

bias) for both cases was not statistically different between the two model configurations, pointing to no obvious change that would impact the statistical performance. For the June and November events, NAM/WRF was statistically better than HRRR/WRF for RMSE (overall error). Overall, the initial and boundary conditions played an important role for the WRF hub height wind prediction, with no clear indication about one preferred set of initial conditions that worked best for all simulated

305   cases. We should note here that the NAM/WRF configuration had one extra nested grid compared to the HRRR/WRF domain setup, which likely contributed to some variation in the 600m domain simulated wind speed. In general, NAM/WRF and HRRR/WRF were capable to describe the low wind speed occurrences, with some under-prediction of higher winds, and difficulty to depict the hub height wind speed increase (but still below the rated wind speed) during the November anticyclone. We further investigated the NAM/WRF and HRRR/WRF model performance differences as related to vertical model levels,

310   SST, and wind power density in the next sections.

315

320

325

330
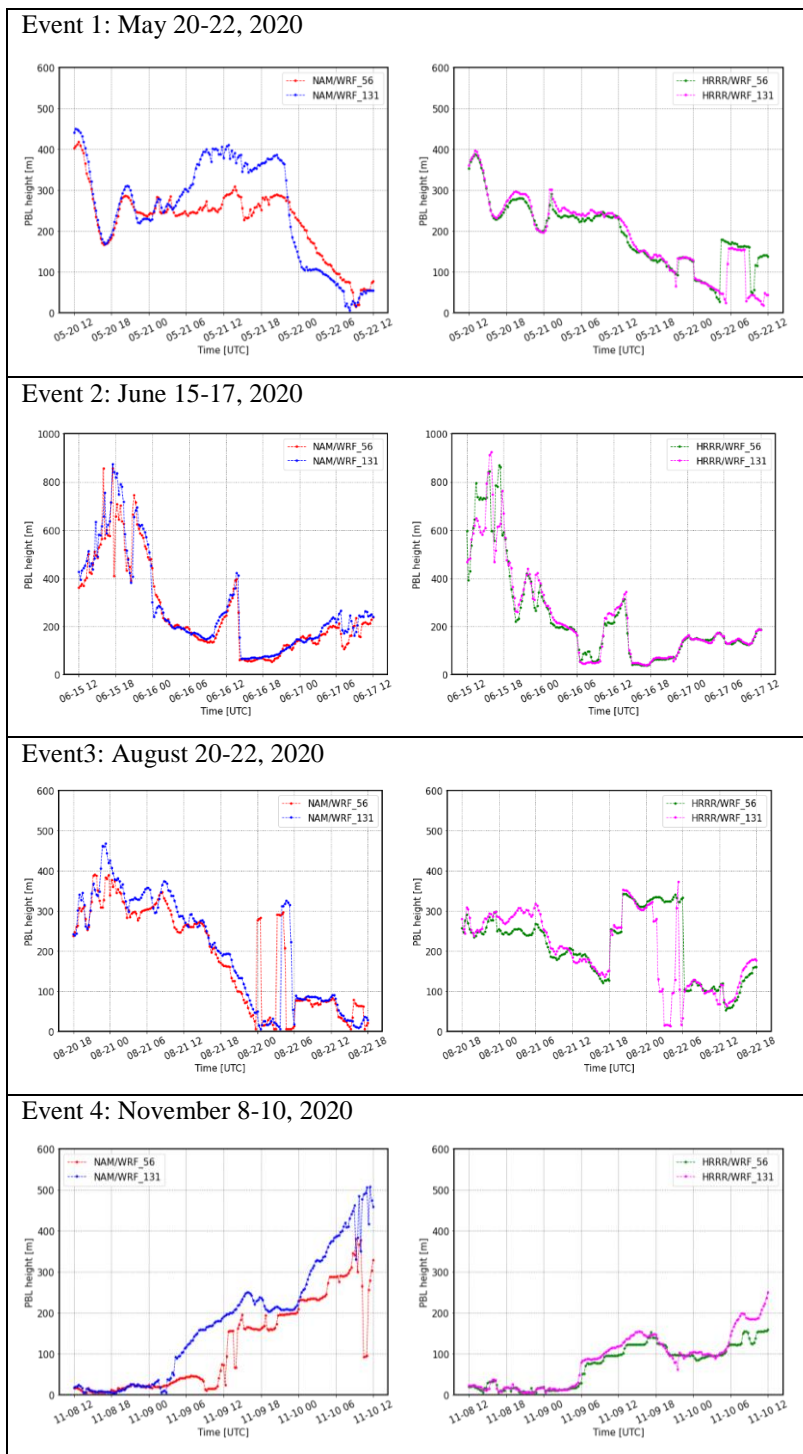
Figure 5: Time series of PBL height from the 600m domain for NAM/WRF and HRRR/WRF and two sets of vertical levels (56 and 131) at the ASIT Lidar Buoy location.
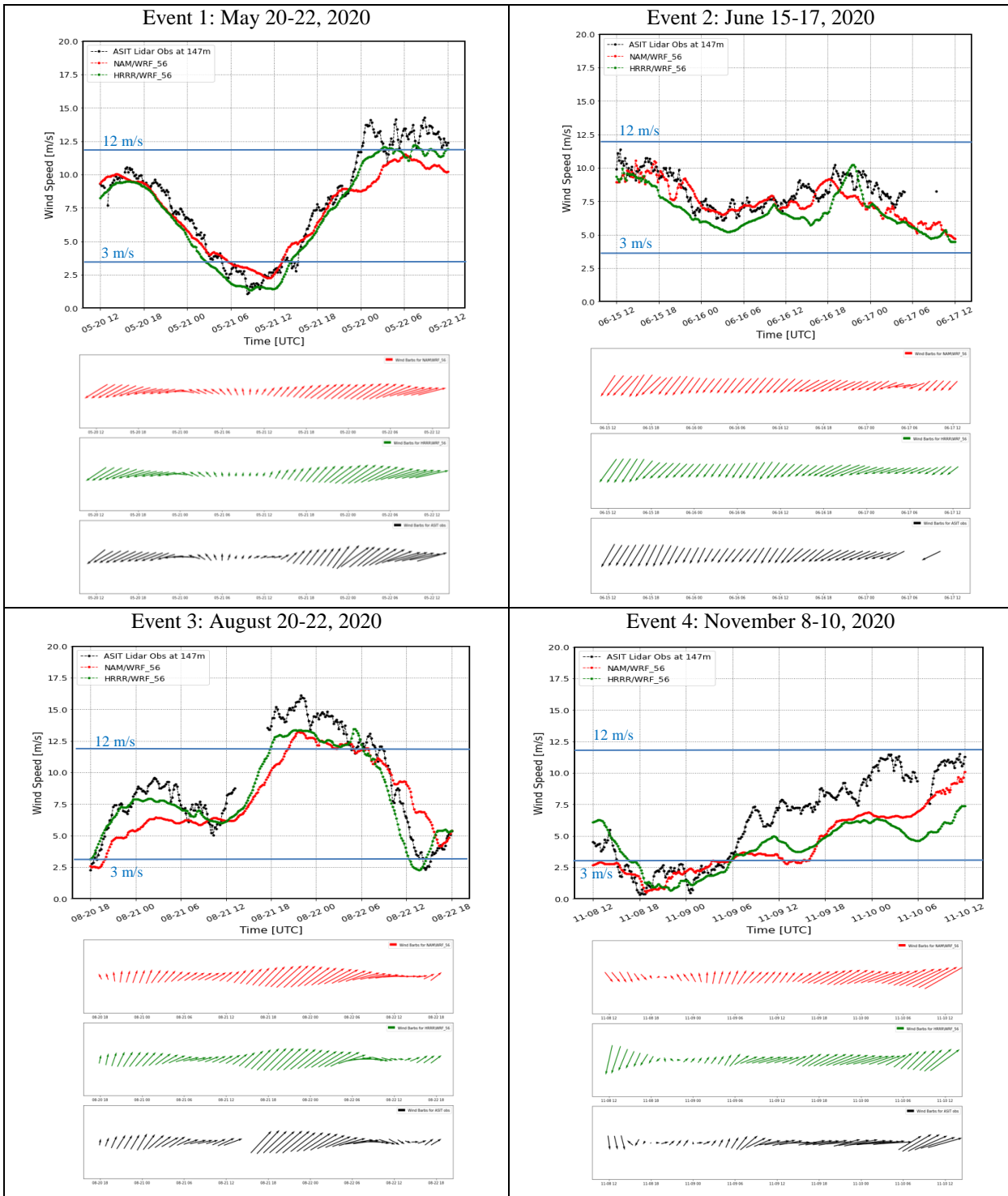
Figure 6: Time series of wind speed and wind direction from Lidar Buoy observations and WRF simulations at the turbine hub height (147 m) (NAM/WRF in red and HRRR/WRF in green color) and 56 vertical levels for the 600 m domain. The blue horizontal lines designate the cut-in and rated wind speeds.

340

3.2 Influence of model vertical levels

We increased the vertical levels up to 400m and added more levels within the boundary layer to investigate the impact in the prediction of hub height wind speed. Bootstrapping confidence intervals for all combinations helped with the assessment of statistical improvement. HRRR/WRF showed less varied PBL heights between simulations with 56 vertical levels versus 131

345 vertical levels compared to NAM/WRF (Fig. 5). For all events, there was no statistically significant change due to adding more vertical levels within the lower boundary layer (Fig. 7). The confidence intervals clearly showed that the influence of the initial and boundary conditions was more important compared to adding more vertical levels (Fig. 7). These results underscored that increasing the vertical resolution did not systematically improve the prediction capability of each model configuration for these four cases.

355
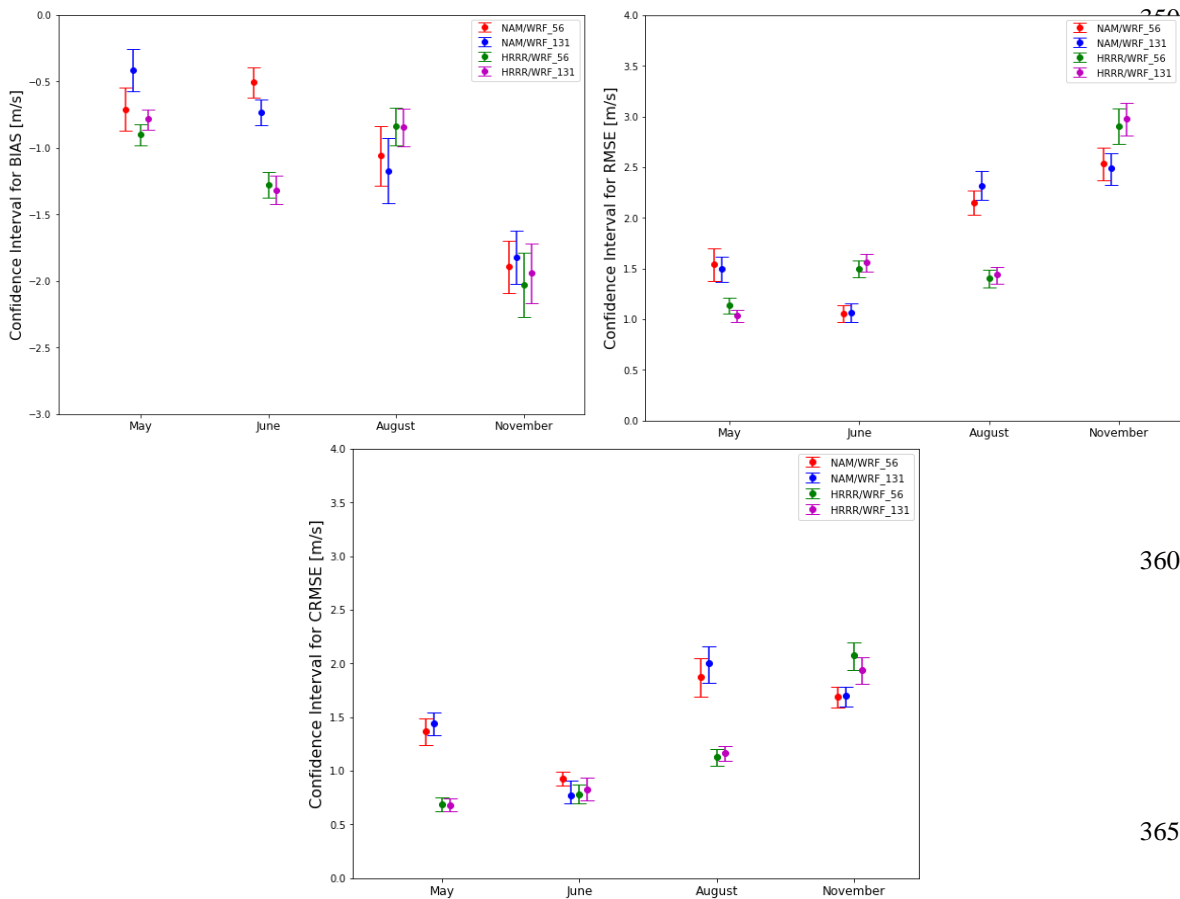
360

365

Figure 7: Bootstrapping confidence intervals for Mean bias, RMSE, and CRMSE of wind speed at 147m height, testing the NAM vs. HRRR initializations and 56 vs 131 vertical levels. Non-overlapping confidence intervals designate statistically different errors.

3.3 Impact of SST

370 Sea surface temperature plays a critical role in the ocean-atmosphere interaction processes through vertical turbulent exchanges of momentum, heat, and moisture (Feng et al. 2022); thus, we assessed its impact on wind prediction capability. To this end, we evaluated two SST products at the observation location. We compared the model SST (NAM and HRRR), and five external SST datasets (OSPO, OSTIA, MUR, NAVO and GOES-16) with the ASIT observation (as mentioned in Section 2.2), to find the SST input that was closest to observations. We decided to use the 5 km OSPO SST product as it best represented the

375 observed SST (Fig. 8). The OSPO product has incorporated data from multiple sources, including satellite imagery and in situ measurements from ships and buoys, to provide accurate and detailed information on SST across the region, while having good coverage over the Northeast U.S. (Maturi et al. 2016).

The SST time series revealed cases where: a) there was substantial deviation in the model SST magnitude compared to the observations, and b) there was available high-resolution SST that matched the observations (Fig. 8). Therefore, of the four

380 anticyclone cases, we selected the May and November cases to further investigate the impact to the hub height winds from a better SST input (Fig. 8). For the August case, the SST from OSPO was close to the NAM and HRRR SST. For the June case, the ASIT tower did not provide SST data. We decided to use the HRRR initialization and 56 vertical levels, as the SST from HRRR exhibited greater deviation from the observations (blue line in Fig.2), and the 131 vertical levels did not significantly improve the results. The change of SST input from HRRR to OSPO for these two simulations did not significantly change the

385 hub height wind speed prediction (Fig. 9). The simulation with OSPO SST tended to correct the time series of wind and bring it closer to the observation during the descending period of wind, while it tended to increase the under-prediction during the rising period of wind for both simulations.
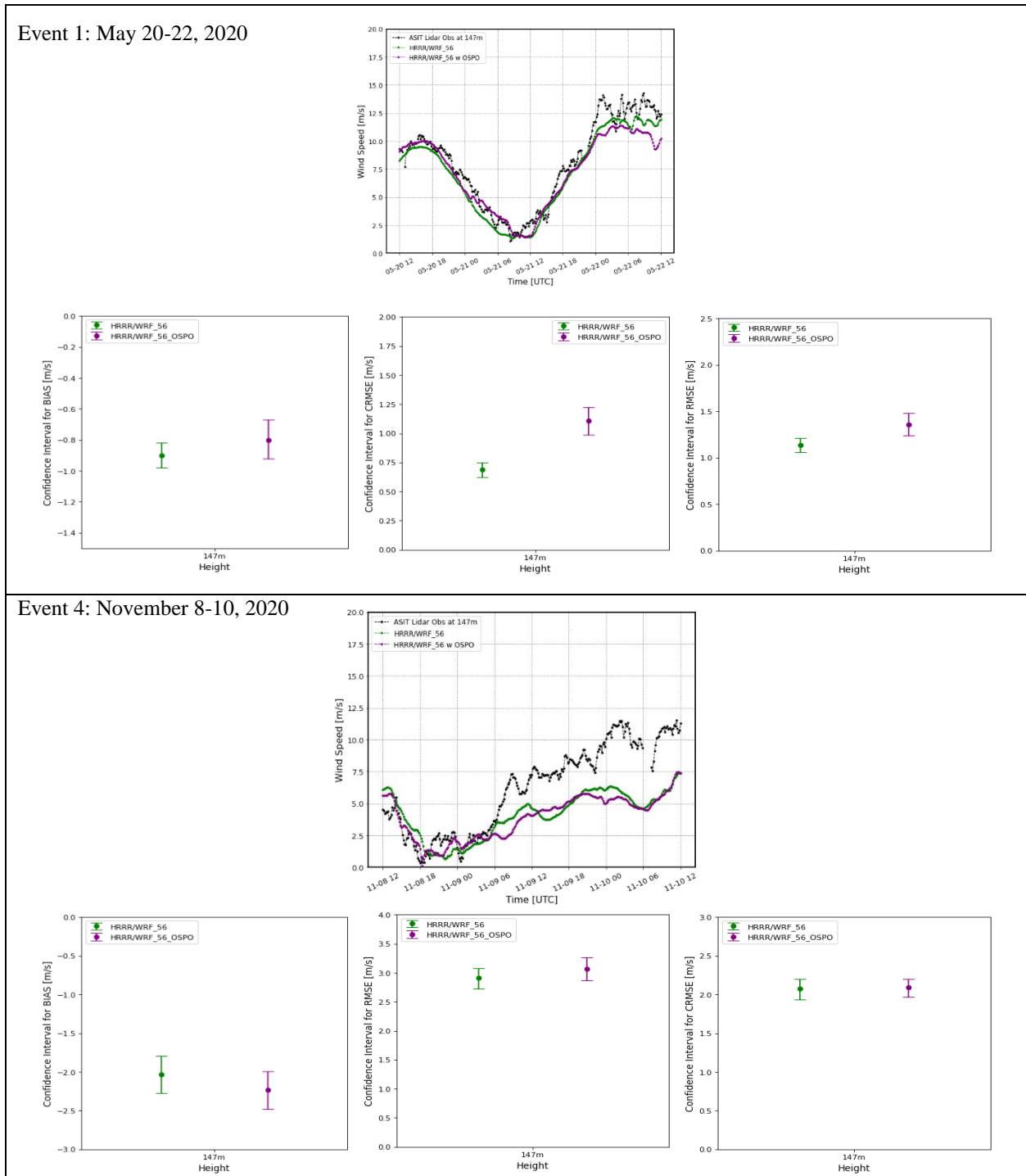
390

395

400
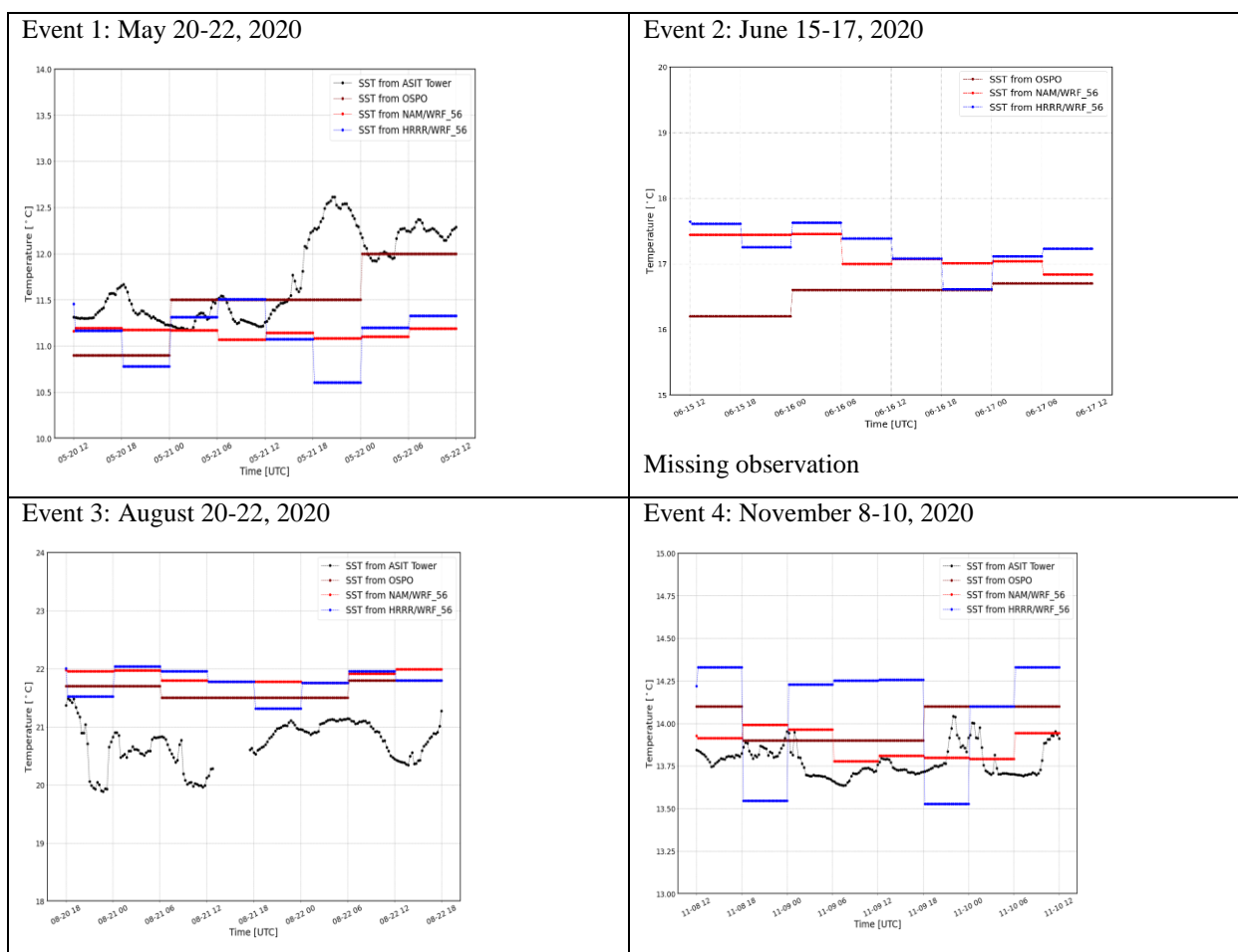
Figure 8: Time series of SST from NAM/WRF and HRRR/WRF with 56 layers, ASIT tower observations and the OSPO product.

Figure 9: Time series of wind speed at the wind turbine hub height from the HRRR/WRF simulations and bootstrapping confidence intervals for Mean bias, RMSE, and CRMSE for the May and November anticyclones. We tested the HRRR initializations with 56 vertical levels and with/without the high-resolution SST input (OSPO 5km).

3.4 Wind power density prediction

From the previous sections, the conclusion was that initial and boundary conditions exhibited the largest influence to the hub
415 height WRF wind prediction. NAM/WRF and HRRR/WRF configurations were able to capture low wind speed occurrences
during the presence and movement of anticyclones, providing confidence that the model is capable to reliably predict such
wind drought occurrences. Even though we selected similar types of weather patterns over the Northeast US (anticyclones
with low wind), there was no single configuration that performed best for all cases. Naturally, the next question was whether
a similar significance would apply to the prediction of offshore wind power density, given that wind power is based on cubic
420 wind speed.

The calculation of Wind Power Density (WPD) (Elliott et al. 1987; Johnson and Erhardt 2016; Martinez and Iglesias, 2022;
Li et al. 2023), which represents the hypothetical wind power content of atmospheric flow, is shown below.
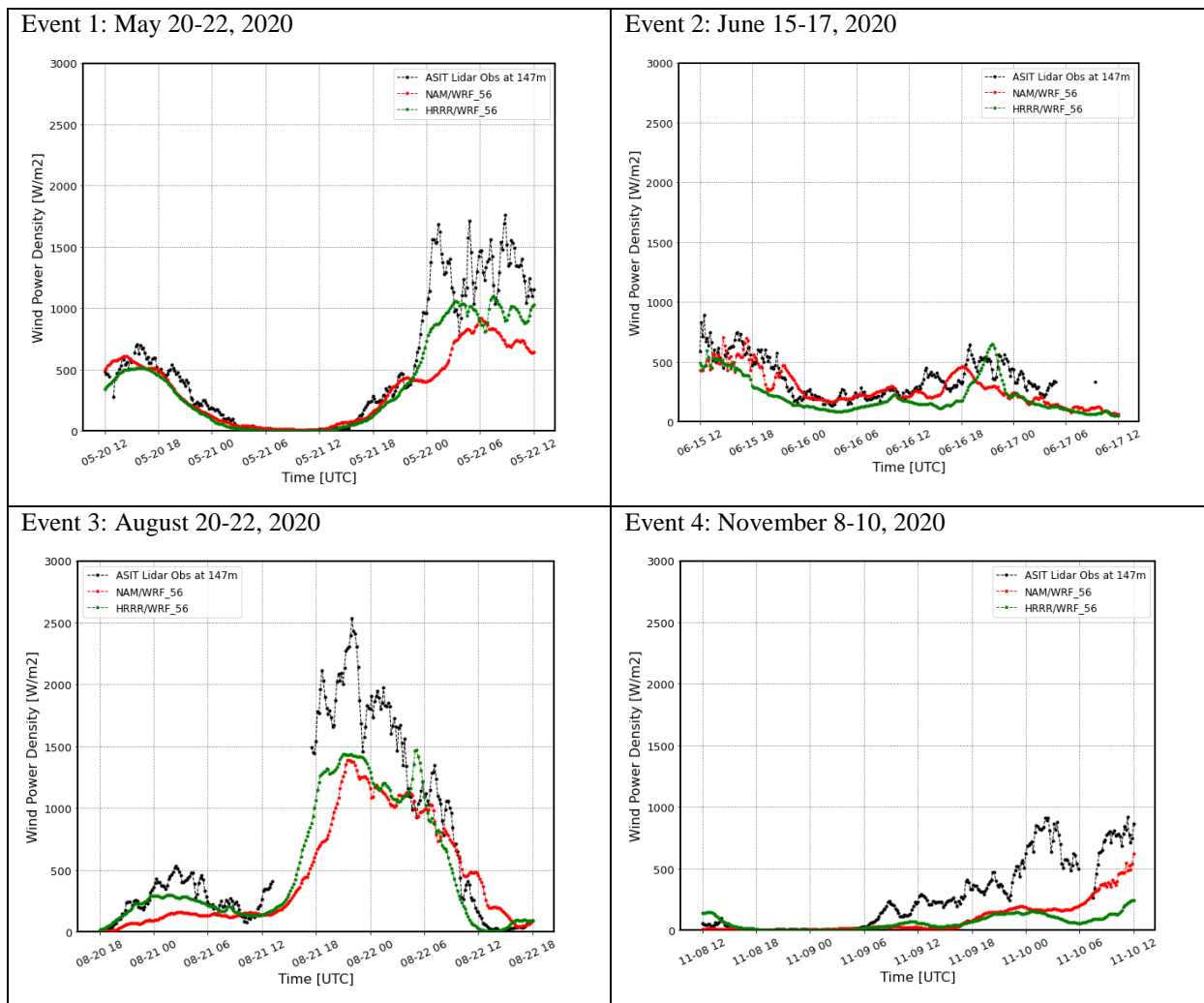
$$\text{Wind Power Density (WPD)} = \frac{1}{2}\rho V^3$$

where ρ is air density (1.207448 kg/m^3), and V wind speed in m/s. The unit of WPD is W/m^2. The calculation of air density
425 included a correction for elevation (Li et.al. 2023, NOAA 1976): $\rho = 1.225 - (1.194 * 10^{-4})Z(\text{station elevation})$

For the selected cases, hub height wind speed did not reach the rated speed of 12 m/s, except for a few hours in May and
August (Fig. 6). This indicated the importance of weakly forced events that produce low wind speed and how they might
influence offshore wind energy production. We plotted time-series of WPD for each event (Fig. 10) to investigate the impact
of wind speed biases on wind power. As the WPD is proportional to cubic wind speed, a small deviation of modeled wind
430 from observations can have a great impact on wind power. This feature was more pronounced for higher wind speeds, as
expected (May and August cases, Fig. 6 and Fig. 10).

The statistically significant difference between WRF model configurations, followed the same patterns as for the hub height
wind speed for the individual events (Fig. 11). For the May and August anticyclones, HRRR/WRF had statistically lower
RMSE and CRMSE compared to NAM/WRF for WPD. For June and November, NAM/WRF showed better error statistics,
435 not consistently for the same metrics though. When testing the confidence of all events together, the HRRR/WRF model
configuration had a significant low model and random error (RMSE & CRMSE) compared to NAM/WRF, while the mean
bias did not exhibit any significant difference. As with hub height wind speed, the difference between vertical levels was
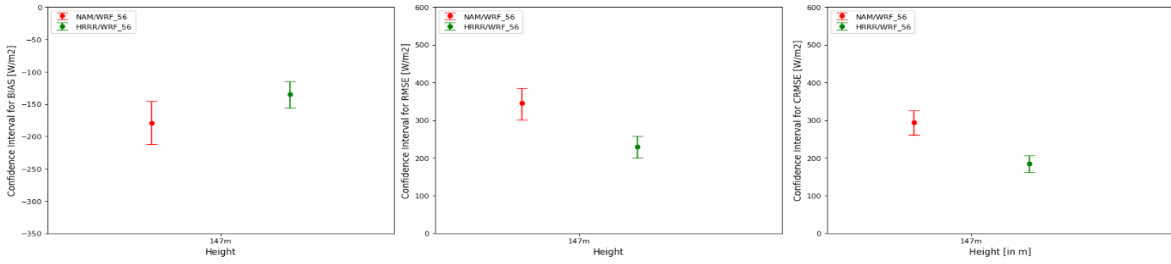insignificant for the WPD error metrics (Fig. 11).

440

Figure 10: Time series of Wind Power Density (WPD in W/m²) from NAM/WRF and HRRR/WRF with 56 layers and ASIT tower observations.
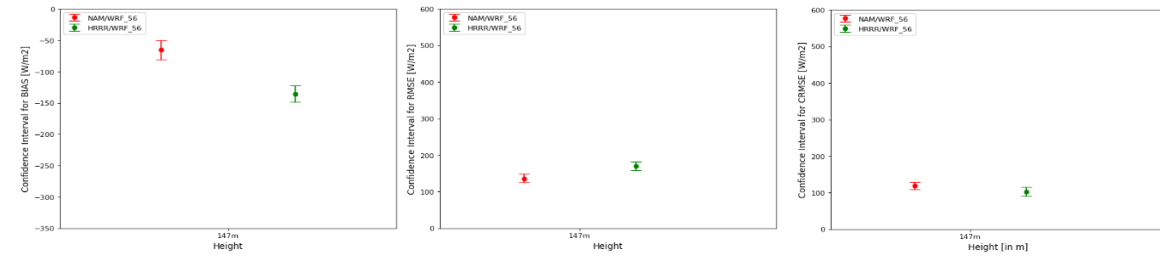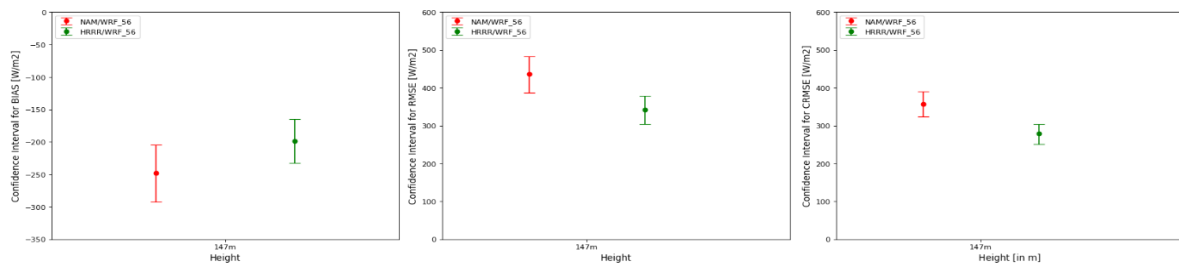
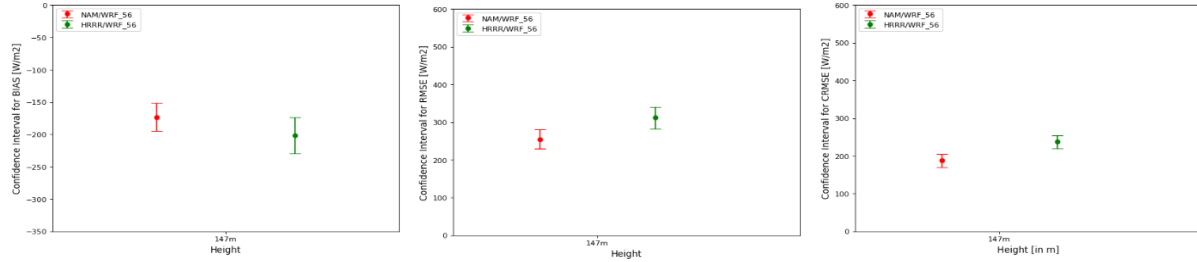## Event 1: May 20-22, 2020

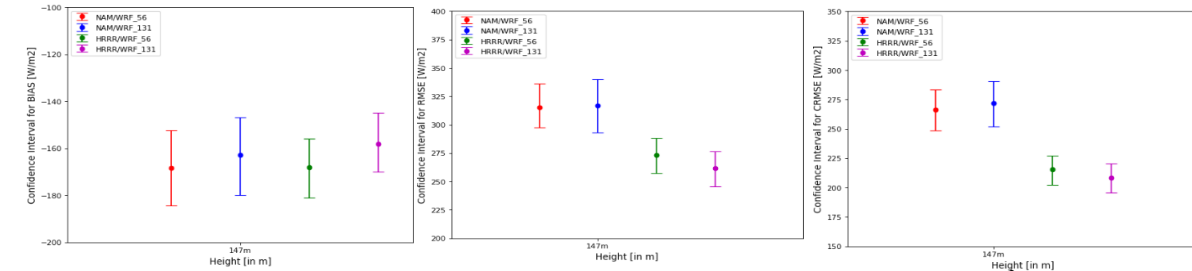## Event 2: June 15-17, 2020

Event 3: August 20-22, 2020

Event 4: November 8-10, 2020

All Events

Figure 11: Bootstrapping confidence intervals for Mean bias, RMSE, and CRMSE of WPD (W/m²). The blue square denotes statistically better error metrics.

4 Concluding remarks

The main objective of this study was to investigate the performance of different WRF model configurations in predicting offshore wind speed and wind power density for anticyclones that coincide with low wind speeds and, thus, underproduction of wind energy. We explored the impact of initial and boundary conditions (NAM versus HRRR), number of vertical layers (56 versus 131), and SST (NAM/HRRR versus OSPO) on hub height wind prediction over the Northeast US cluster of wind farm lease areas. The only available offshore measurements at the time of the study came from the WHOI's ASIT tower which was adjacent and not directly inside the intended leased area of the offshore wind farm. This resulted in configuring the WRF modeling domains to include the tower location for model evaluation purposes.

We used SOMs to objectively select events that shared similar synoptic-scale conditions. We selected events of a similar type, originating from the same SOM node, that exhibited relatively weak winds coming from similar directions (northwesterly winds for events under node 7 and southerly winds for events under node 12). The maps also aided in identifying events with relatively weak forcing due to the regional pressure gradient which translated in wind below the wind turbine rated wind speed limit. As the rated wind speed represents the operational condition of the wind farm, it is very important for NWP models to accurately predict events with weak forcing when they are persistent in time.

Overall, the performance of the WRF model in predicting offshore wind at hub-height during the influence of anticyclones was primarily influenced by initial and boundary conditions. Adding model vertical levels did not change the model performance significantly and consistently. Another important factor to consider was the SST that could impact atmospheric stability and air-sea fluxes, as variations in SST affect the stability of the marine boundary layer and thus the generation of offshore winds. The OSPO SST was closer to the actual observed SST and corrected part of the wind profile for two of the selected cases, but it didn't provide any significant improvement in the error statistics.

There was not a single model configuration that consistently gave statistically better hub height wind speed predictions, and when wind speed translated to wind power density, the statistics remained the same. Individually, wind power density was better predicted by HRRR/WRF for the May and August anticyclones, while NAM/WRF had better error statistics for the June and November events. The HRRR/WRF configuration showed significantly lower RMSE (266-316 W/m^2) and CRMSE (208-266 W/m^2) compared to NAM/WRF, when we considered all four events together. Our work underscored that for predicting offshore wind resources, it is important to evaluate not only the WRF predictive wind speed, but also the connection of wind speed to wind power. The long-term goal of this project is to deploy WRF operationally for the NE US wind farms by choosing the best potential configuration. Future work includes the expansion of WRF simulations for other offshore meteorological conditions that are important for offshore wind energy forecasting, such as low-pressure systems, cold fronts, and presence of low-level jets.

Code and data availability

Offshore wind speed observations are taken from the Air-Sea Interaction Tower (ASIT) archived at the Woods Hole
520 Oceanographic Institution's (WHOI), and are publicly accessible. SST data are also publicly available from the 0.054º Office
of Satellite and Product Operations (OSPO) analysis dataset. The WRF model is a community modeling system and its code
is freely available to the public. We have used the open-source Python package, minisom, to create the Self Organizing Maps.
We acknowledge the North American Mesoscale Forecast System (NAM), and the High-Resolution Rapid Refresh (HRRRv3)
model, for the initialization for our WRF simulations.

525 **Author contribution**

TZ and MA conceptualized the research topic. TZ, MA, TJ, PH designed the modelling experiments and TZ carried them out.
TZ was responsible for validation, visualization, and writing of the article. TZ edited the manuscript with contributions from
all co-authors. MA supervised the research activity and execution.

530 **Competing interests**

The authors declare that they have no conflict of interest.

Acknowledgements

References

Aird, J. A., Barthelmie, R. J., Shepherd, T. J., and Pryor, S. C.: Occurrence of Low-Level Jets over the Eastern U.S. Coastal
Zone at Heights Relevant to Wind Energy, Energies (Basel), 15, 445, https://doi.org/10.3390/en15020445, 2022.

540 Anon: New York Wind Energy Guide for Local Decision Makers: Wind Energy Basics, n.d. https://www.nyserda.ny.gov/All-Programs/Clean-Energy-Siting-Resources/Wind-Guidebook

Archer, C. L., Colle, B. A., Veron, D. L., Veron, F., and Sienkiewicz, M. J.: On the predominance of unstable atmospheric
conditions in the marine boundary layer offshore of the U.S. northeastern coast, Journal of Geophysical Research:
545 Atmospheres, 121, 8869–8885, https://doi.org/10.1002/2016JD024896, 2016.

Banta, R. M., Pichugina, Y. L., Brewer, W. A., James, E. P., Olson, J. B., Benjamin, S. G., Carley, J. R., Bianco, L., Djalalova, I. V., Wilczak, J. M., Hardesty, R. M., Cline, J., and Marquis, M. C.: Evaluating and Improving NWP Forecast Models for the Future: How the Needs of Offshore Wind Energy Can Point the Way, Bull Am Meteorol Soc, 99, 1155–1176, https://doi.org/10.1175/BAMS-D-16-0310.1, 2018.

550

Baring-Gould, I.: Overview of Current Wind Energy Technologies BOEM Offshore Renewable Energy Workshop, n.d. https://www.boem.gov/sites/default/files/about-boem/BOEM-Regions/Pacific-Region/Renewable-Energy/4-Ian-Baring-Gould---Wind-Technology-Overview.pdf

555

Benjamin, S. G., Weygandt, S. S., Brown, J. M., Hu, M., Alexander, C. R., Smirnova, T. G., Olson, J. B., James, E. P., Dowell, D. C., Grell, G. A., Lin, H., Peckham, S. E., Smith, T. L., Moninger, W. R., Kenyon, J. S., and Manikin, G. S.: A North American Hourly Assimilation and Model Forecast Cycle: The Rapid Refresh, Mon Weather Rev, 144, 1669–1694, https://doi.org/10.1175/MWR-D-15-0242.1, 2016a.

560

Bodini, N., Lundquist, J. K., and Kirincich, A.: U.S. East Coast Lidar Measurements Show Offshore Wind Turbines Will Encounter Very Low Atmospheric Turbulence, Geophys Res Lett, 46, 5582–5591, https://doi.org/10.1029/2019GL082636, 2019.

565 Colle, B. A., Sienkiewicz, M. J., Archer, C., Veron, D., Veron, F., Kempton, W., and Mak, J. E.: Improving the Mapping and Prediction of Offshore Wind Resources (IMPOWR): Experimental Overview and First Results, Bull Am Meteorol Soc, 97, 1377–1390, https://doi.org/10.1175/BAMS-D-14-00253.1, 2016.

Costoya, X., deCastro, M., Carvalho, D., and Gómez-Gesteira, M.: On the suitability of offshore wind energy resource in the
570 United States of America for the 21st century, Appl Energy, 262, 114537, https://doi.org/10.1016/J.APENERGY.2020.114537, 2020.

Debnath, M., Doubrawa, P., Optis, M., Hawbecker, P., and Bodini, N.: Extreme wind shear events in US offshore wind energy areas and the role of induced stratification, Wind Energy Science, 6, 1043–1059, https://doi.org/10.5194/WES-6-1043-2021,
575 2021.

Draxl, C., Hodge, B. M., Clifton, A., and McCaa, J.: Overview and Meteorological Validation of the Wind Integration National Dataset toolkit, https://doi.org/10.2172/1214985, 2015.

580   Elliott, D. L., Holladay, C. G., Barchet, W. R., Foote, H. P., and Sandusky, W. F.: Wind Energy Resource Atlas of the United States Wind Energy Resource Atlas of the United States Wind Energy Resource Atlas of the United States, n.d.

EPRI: Historical Trends and Projected Changes in U.S. Wind and Solar Resources. EPRI, Palo Alto, CA: 2021. 3002020619, 2021

585

Feng, Y., Gao, Z., Xiao, H., Yang, X., and Song, Z.: Predicting the Tropical Sea Surface Temperature Diurnal Cycle Amplitude Using an Improved XGBoost Algorithm, Journal of Marine Science and Engineering 2022, Vol. 10, Page 1686, 10, 1686, https://doi.org/10.3390/JMSE10111686, 2022.

590   Filippelli, M.V., Markus, M., Eberhard, M., Bailey, B.H. and Dubois, L.: Metocean data needs assessment and data collection strategy development for the Massachusetts wind energy area Tech. rep. URL http://files. masscec. com/research/wind/MassCECMetoceanDataReport. Pdf, 2015.

Floors, R., Vincent, C.L., Gryning, S.E., Peña, A. and Batchvarova, E: The wind profile in the coastal boundary layer: Wind
595   lidar measurements and numerical modelling. Boundary-layer meteorology, 147, pp.469-491, 2013.

Hallgren, C., Arnqvist, J., Ivanell, S., Körnich, H., Vakkari, V., and Sahlée, E.: Looking for an Offshore Low-Level Jet Champion among Recent Reanalyses: A Tight Race over the Baltic Sea, Energies 2020, Vol. 13, Page 3670, 13, 3670, https://doi.org/10.3390/EN13143670, 2020.

600

Haupt, S. E., Kosović, B., Berg, L. K., Kaul, C. M., Churchfield, M., Mirocha, J., Allaerts, D., Brummet, T., Davis, S., Decastro, A., Dettling, S., Draxl, C., Gagne, D. J., Hawbecker, P., Jha, P., Juliano, T., Lassman, W., Quon, E., Rai, R. K., Robinson, M., Shaw, W., and Thedin, R.: Lessons learned in coupling atmospheric models across scales for onshore and offshore wind energy, Wind Energy Science (Online), 8, 1251–1275, https://doi.org/10.5194/WES-8-1251-2023, 2023.

605

Hawbecker, P. and Knievel, J. C.: Simulating the Chesapeake Bay Breeze: Sensitivities to Water Surface Temperature, J Appl Meteorol Climatol, 61, 1595–1611, https://doi.org/10.1175/JAMC-D-22-0002.1, 2022.
https://www.energy.gov/eere/wind/wind-market-reports-2023-edition

610   James, E. P., Benjamin, S. G., and Marquis, M.: Offshore wind speed estimates from a high-resolution rapidly updating numerical weather prediction model forecast dataset, Wind Energy, 21, 264–284, https://doi.org/10.1002/WE.2161, 2018.

Johnson, D. L., R. J. Erhardt: Projected impacts of climate change on wind energy density in the United States, Renewable Energy, Volume 85, 2016, Pages 66-73, ISSN 0960-1481, https://doi.org/10.1016/j.renene.2015.06.005, 2016.

615

JPL MUR MEaSUREs Project – GHRSST Level 4 MUR 0.25 deg Global Foundation Sea Surface Temperature Analysis (v.4.2), PO. DAAC, CA, USA, https://doi.org/10.5067/GHM25-4FJ42, 2019.

Juliano, T. W. and Lebo, Z. J.: Linking large-scale circulation patterns to low-cloud properties, Atmos Chem Phys, 20, 7125–
620 7138, https://doi.org/10.5194/ACP-20-7125-2020, 2020.

Kempton, W., Pimenta, F. M., Veron, D. E., and Colle, B. A.: Electric power from offshore wind via synoptic-scale interconnection, Proc Natl Acad Sci U S A, 107, 7240–7245, https://doi.org/10.1073/PNAS.0909075107/SUPPL_FILE/PNAS.0909075107_SI.PDF, 2010.

625

Kirincich, Anthony R., "2020 Lidar summary data", 2020, https://hdl.handle.net/1912/27206

Kohonen, T.: The Basic SOM, 77–130, https://doi.org/10.1007/978-3-642-97610-0_3, 1995.

630 Li, H., Claremar, B., Wu, L., Hallgren, C., Körnich, H., Ivanell, S., and Sahlée, E.: A sensitivity study of the WRF model in offshore wind modeling over the Baltic Sea, Geoscience Frontiers, 12, 101229, https://doi.org/10.1016/j.gsf.2021.101229, 2021.

Li, Z., Wan, B., Duan, Z., He, Y., Yu, Y., and Chen, H.: Evaluation of HY-2C and CFOSAT Satellite Retrieval Offshore Wind
635 Energy Using Weather Research and Forecasting (WRF) Simulations, Remote Sens (Basel), 15, 4172, https://doi.org/10.3390/rs15174172, 2023.

Liu, B., Costa, K. B., Xie, L., and Semazzi, F. H. M.: Dynamical downscaling of climate change impacts on wind energy resources in the contiguous United States by using a limited-area model with scale-selective data assimilation, Advances in
640 Meteorology, 2014, https://doi.org/10.1155/2014/897246, 2014.

Martinez, A. and Iglesias, G.: Climate change impacts on wind energy resources in North America based on the CMIP6 projections, Science of The Total Environment, 806, 150580, https://doi.org/10.1016/J.SCITOTENV.2021.150580, 2022.

645 Maturi, Eileen; Sapper, John; Harris, Andy; Mittaz, Jonathan (2016). GHRSST Level 4 OSPO Global Foundation Sea Surface Temperature Analysis (GDS version 2). [indicate subset used]. NOAA National Centers for Environmental Information.

Musial, W., Spitsen, P., Beiter, P., Duffy, P., Marquis, M., Cooperman, A., Hammond, R., and Shields, M.: Offshore Wind Market Report: 2021 Edition, https://doi.org/10.2172/1818842, 2021.

650

National Oceanic and Atmospheric Administration (NOAA). 1976. U. S. Standard Atmosphere. NOAAS/T76-1562, Washington, DC.

Naval Oceanographic Office. METOP-A AVHRR GAC L2P swath SST dataset v2.0. Ver. 2.0. PO.DAAC, CA, USA, https://doi.org/10.5067/10.5067/GHMTA-2PN20

655

Niu, G. Y., Yang, Z. L., Mitchell, K. E., Chen, F., Ek, M. B., Barlage, M., Kumar, A., Manning, K., Niyogi, D., Rosero, E., Tewari, M., and Xia, Y.: The community Noah land surface model with multiparameterization options (Noah-MP): 1. Model description and evaluation with local-scale measurements, Journal of Geophysical Research: Atmospheres, 116, 12109, https://doi.org/10.1029/2010JD015139, 2011.

660

NOAA/NESDIS/STAR. GHRSST L3C ACSPO America Region SST from GOES-16 ABI . Ver. 2.70. PO.DAAC, CA, USA. accessed [YYYY-MM-DD] at 10.5067/GHG16-3UO27

665 Nunalee, C. G. and Basu, S.: Mesoscale modeling of coastal low-level jets: implications for offshore wind resource estimation, Wind Energy, 17, 1199–1216, https://doi.org/10.1002/WE.1628, 2014.

Office of Satellite Products and Operations. GHRSST Level 4 NOAA/OSPO Global Sea Surface Foundation Temperature. Ver. 1.0. PO.DAAC, CA, USA. accessed [YYYY-MM-DD] at 10.5067/GHGPB-4FO02

670

Optis, M., Kumler, A., Brodie, J., and Miles, T.: Quantifying sensitivity in numerical weather prediction-modeled offshore wind speeds through an ensemble modeling approach, Wind Energy, 24, 957–973, https://doi.org/10.1002/WE.2611, 2021.

Pryor, S. C. and Barthelmie, R. J.: Statistical analysis of flow characteristics in the coastal zone, Journal of Wind Engineering 675 and Industrial Aerodynamics, 90, 201–221, https://doi.org/10.1016/S0167-6105(01)00195-7, 2002.

Pryor, S. C., Barthelmie, R. J., and Schoof, J. T.: Past and future wind climates over the contiguous USA based on the North American Regional Climate Change Assessment Program model suite, J. Geophys. Res, 117, 19119, https://doi.org/10.1029/2012JD017449, n.d.

680

Rai, R. K., Berg, L. K., Kosović, B., Haupt, S. E., Mirocha, J. D., Ennis, B. L., and Draxl, C.: Evaluation of the impact of horizontal grid spacing in terra incognita on coupled mesoscale-microscale simulations using the WRF framework, Mon Weather Rev, 147, 1007–1027, https://doi.org/10.1175/MWR-D-18-0282.1, 2019.

685 Redfern, S., Optis, M., Xia, G., and Draxl, C.: Offshore wind energy forecasting sensitivity to sea surface temperature input in the Mid-Atlantic, Wind Energy Science, 8, 1–23, https://doi.org/10.5194/WES-8-1-2023, 2023.

Ryu, G.-H., Kim, D.-H., Lee, H.-W., Park, S.-Y., and Kim, H.-G.: A Study of Energy Production Change according to Atmospheric Stability and Equivalent Wind Speed in the Offshore Wind Farm using CFD Program, Journal of Environmental
690 Science International, 25, 247–257, https://doi.org/10.5322/JESI.2016.25.2.247, 2016.

Skamarock, W.C., Klemp, J.B., Dudhia, J., Gill, D.O., Liu, Z., Berner, J., Wang, W., Powers,
J.G., Duda, M.G., Barker, D.M. and Huang, X.Y.: A description of the advanced
research WRF model version 4. National Center for Atmospheric Research: Boulder, CO,
695 USA, 145(145), p.550, 2019.

Skamarock, W. C. and Klemp, J. B.: A time-split nonhydrostatic atmospheric model for weather research and forecasting applications, J Comput Phys, 227, 3465–3485, https://doi.org/10.1016/J.JCP.2007.01.037, 2008.

700 Skamarock, W. C., Klemp, J. B., Dudhia, J., Gill, D. O., Barker, D. M., Wang, W., and Powers, J. G.: A Description of the Advanced Research WRF Version 2, 2005.

Stauffer, R. M., Thompson, A. M., and Young, G. S.: Tropospheric ozonesonde profiles at long-term U.S. monitoring sites: 1. A climatology based on self-organizing maps, Journal of Geophysical Research: Atmospheres, 121, 1320–1339,
705 https://doi.org/10.1002/2015JD023641, 2016.

Svensson, N., Arnqvist, J., Bergström, H., Rutgersson, A., and Sahlée, E.: Measurements and Modelling of Offshore Wind Profiles in a Semi-Enclosed Sea, Atmosphere 2019, Vol. 10, Page 194, 10, 194, https://doi.org/10.3390/ATMOS10040194, 2019a.
710

Svensson, N., Bergström, H., Rutgersson, A., and Sahlée, E.: Modification of the Baltic Sea wind field by land-sea interaction, Wind Energy, 22, 764–779, https://doi.org/10.1002/WE.2320, 2019b.

UK Met Office. GHRSST Level 4 OSTIA Global Reprocessed Foundation Sea Surface Temperature Analysis (GDS2). Ver.

715   2.0. PO.DAAC, CA, USA. accessed [YYYY-MM-DD] at 10.5067/GHOST-4RM02

US DOE, EERE, 2023: Offshore Wind Market Report: 2023 Edition.

Vickers, D. and Mahrt, L.: Observations of non-dimensional wind shear in the coastal zone, Quarterly Journal of the Royal

720   Meteorological Society, 125, 2685–2702, https://doi.org/10.1002/qj.49712555917, 1999.

Wang, D., Jensen, M. P., Taylor, D., Kowalski, G., Hogan, M., Wittemann, B. M., Rakotoarivony, A., Giangrande, S. E., and Park, J. M.: Linking Synoptic Patterns to Cloud Properties and Local Circulations Over Southeastern Texas, Journal of Geophysical Research: Atmospheres, 127, https://doi.org/10.1029/2021JD035920, 2022.

725

Yoo, J.-W., Lee, H.-W., Lee, S.-H., and Kim, D.-H.: Characteristics of Vertical Variation of Wind Resources in Planetary Boundary Layer in Coastal Area using Tall Tower Observation, Journal of Korean Society for Atmospheric Environment, 28, 632–643, https://doi.org/10.5572/KOSAE.2012.28.6.632, 2012.